AFRL-AFOSR-VA-TR-2024-0168

Materials with designed nonlinearities: enabling a new generation of stress wave transformation

Boechler, Nicholas
UNIVERSITY OF WASHINGTON
4333 BROOKLYN AVE NE
SEATTLE, WA, 98195
USA

02/19/2024
Final Technical Report

Air Force Research Laboratory
Air Force Office of Scientific Research
Arlington, Virginia 22203
Air Force Materiel Command

REPORT DOCUMENTATION PAGE

PLEASE DO NOT RETURN YOUR FORM TO THE ABOVE ORGANIZATION.

1. REPORT DATE	2. REPORT TYPE	3. DATES COVERED	
20240219	Final	START DATE 20160930	END DATE 20200929

4. TITLE AND SUBTITLE
Materials with designed nonlinearities: enabling a new generation of stress wave transformation

5a. CONTRACT NUMBER	5b. GRANT NUMBER	5c. PROGRAM ELEMENT NUMBER
	FA9550-16-1-0142	61102F
5d. PROJECT NUMBER	**5e. TASK NUMBER**	**5f. WORK UNIT NUMBER**

6. AUTHOR(S)
Nicholas Boechler

7. PERFORMING ORGANIZATION NAME(S) AND ADDRESS(ES)
UNIVERSITY OF WASHINGTON
4333 BROOKLYN AVE NE
SEATTLE, WA 98195
USA

8. PERFORMING ORGANIZATION REPORT NUMBER

9. SPONSORING/MONITORING AGENCY NAME(S) AND ADDRESS(ES)	10. SPONSOR/MONITOR'S ACRONYM(S)	11. SPONSOR/MONITOR'S REPORT NUMBER(S)
Air Force Office of Scientific Research 875 N. Randolph St. Room 3112 Arlington, VA 22203	AFRL/AFOSR RTA1	AFRL-AFOSR-VA-TR-2024-0168

12. DISTRIBUTION/AVAILABILITY STATEMENT
A Distribution Unlimited: PB Public Release

13. SUPPLEMENTARY NOTES

14. ABSTRACT
Material nonlinearity is potentially one of the most transformative, yet underexplored, methods for controlling stress wave propagation. The objective of this AFOSR Young Investigator Program proposal is to answer the following fundamental open questions: “how can we create materials with any desired material nonlinearity?; “what material nonlinearity is the best for a given dynamic loading scenario?; and what situation-specific nonlinearity enables the translation of a given dynamic input to any desired dynamic output?” To answer these questions, we will utilize additively manufactured, microstructured lattice materials as a
flexible, structural toolbox for developing and studying materials with designed, effective material nonlinearities stemming from microstructural geometric nonlinearities. This study will truly be revolutionary, causing a paradigm shift away from studies of dynamical systems containing specific material nonlinearities, and will open a new class of ultralight materials with tailorable nonlinearity and extraordinary stress wave transformation properties.

15. SUBJECT TERMS

16. SECURITY CLASSIFICATION OF:			17. LIMITATION OF ABSTRACT	18. NUMBER OF PAGES
a. REPORT U	b. ABSTRACT U	c. THIS PAGE U	UU	29

19a. NAME OF RESPONSIBLE PERSON	19b. PHONE NUMBER *(Include area code)*
DEREK BARBEE	000-0000

Standard Form 298 (Rev.5/2020)
Prescribed by ANSI Std. Z39.18

Technical Specifications/References: "Materials with designed nonlinearities: enabling a new generation of stress wave transformation" Grant no. FA9550-16-1-0142, PI: Nicholas Boechler

We summarize here the contributions made over the course of the grant.

Students supported:

- Maroun Abi Ghanem. Maroun was a postdoctoral scholar and project scientist in the PI's research group. Maroun led the fabrication of microstructured material samples, helped with the development of an optimization framework to find microstructural unit cell geometries that match desired force-displacement laws, and led the dynamic testing of microstructured material samples.
- Reza Behrou. Reza was a postdoctoral researcher in the PI's research group. Reza led the development of the new topology and shape optimization framework, and led the optimization studies for tailored nonlinear constitutive responses.
- Samuel Wallen. Sam was a PhD student in the PI's research group, and graduated with his Ph.D. in June 2017. Sam contributed to the project by setting up a flexible framework wherein nonlinear discrete element simulations could be conducted with variable nearest-neighbor force-displacement laws.

Students contributing to the project, but not supported by the grant:

- Carlos Guerrero. Carlos was a summer visiting undergraduate researcher supported by the UCSD ENLACE program. She contributed to developing improved microstructured lattice manufacturing techniques.
- Diego Garcia. Diego was a summer visiting undergraduate researcher from Mexico supported by the UCSD ENLACE program. He contributed to developing improved microstructured lattice manufacturing techniques.
- Brianna MacNider. UCSD PhD student. She contributed to the mechanical testing of lattice samples shown in the manuscript attached.
- Vimarsh Verma. UCSD Masters student. Contributed to the mechanical testing of lattice samples shown in the manuscript attached below.
- Ryan Alvey. UCSD undergraduate student. Contributed to the mechanical testing of lattice samples shown in the manuscript attached below.
- Jinho Hong. UCSD undergraduate student. Contributed to the mechanical testing of lattice samples shown in the manuscript attached below.
- Mariana Avila. Mariana was a summer visiting undergraduate researcher from Mexico supported by the UCSD ENLACE program. She contributed to developing improved microstructured lattice manufacturing techniques.
- Pedro Levya. Pedro was a summer visiting undergraduate researcher from Mexico supported by the UCSD ENLACE program. He contributed to developing improved microstructured lattice manufacturing techniques.
- Ariana Mendible. Ariana was supported by the University of Washington through a Graduate Opportunities and Minority Achievement Program (GO-MAP) fellowship for the first academic year. Ariana worked on: conducting parametric studies varying the nonlinear force-displacement law in our discrete element model simulation, the fabrication of microstructured material samples, development of an optimization framework to find microstructural unit cell

geometries that match desired force-displacement laws, and dynamic testing of microstructured material samples.

- Morgan Bassford. Morgan was a Masters student in the PI's research group. Morgan graduated with her Masters degree in June 2017. In her contributions to the project, she conducted: the initial fabrication and mechanical testing of microstructured materials, the initial heuristic microstructure design for lattice materials with tailored nonlinear responses, and the initial attempts at optimization of the unit cell microstructural geometry.
- Samuel Merritt. Samuel was a Masters student in the PI's research group and graduated with his Masters degree in December 2016, was supported by the GI Bill, and contributed to the development of the initial microstructure optimization algorithms.
- Tim Brummer. Tim was a Masters student in the PI's research group, and contributed to the development of the initial microstructure optimization algorithms.
- Vinod Ramakrishnan. Vinod was a visiting undergraduate student from IIT Gandhinagar, who assisted Ariana and Maroun on their project efforts.

Faculty collaborators on the project:

- Alicia Kim (University of California, San Diego): Collaboration in developing the optimization framework.
- Ashley Emery (University of Washington): Central contributions to developing a gradient-based microstructure optimization framework.
- Richard Wiebe (University of Washington): Useful discussion on nonlinear finite element modeling.
- Josh Hamel (Seattle University): Useful discussions on optimization approaches.

Presentations related to the project:

- Bassford, M., Bhosale, S., Merritt, S., Brummer, T., Mendible, A., Abi Ghanem, M., Wallen, S. P., and Boechler, N., "Dynamics of materials with tailorable, microstructure-enabled nonlinearities", Phononics 2017: The 4th international conference on phononic crystals/metamaterials, phonon transport/coupling and topological phononics, pp. 82-83, Changsha, China (6/2017)
- Boechler, N., "Microstructural mechanisms for tailoring effective material nonlinear dynamic response", SIAM Conference on Applications of Dynamical Systems, DS17 Abstracts, pp. 143, Snowbird, UT (5/2017)
- Boechler, N., "Dynamics of materials with designed microstructures: towards self- assembled energetic materials with tailored dynamic responses", Biannual Purdue Energetic Materials Summit (PEMS), West Lafayette, IN (5/2017)
- Boechler, N., "Dynamics of nonlinear lattices and surface instabilities in soft materials", Elastic Metamaterials Group Meeting, Le Mans University, France (6/2018)
- Northwestern University, Scaling down (and up) dynamically responsive materials, Theoretical and Applied Mechanics Seminar (1/2019)
- Rice University, Engineering material responsivity: the importance of being simultaneously small and large, Department of Mechanical Engineering Seminar (4/2019)
- University of California, San Diego, 2nd Calibaja Symposium and Workshop, Dynamically responsive materials: the importance of simultaneously small, big, and very nonlinear structure (5/2019)

- Boechler, N., “Recent Progress in Tuning the Dynamic Response of Non-linear Metastructures”, Phononics 2019: 5th International Conference on Phononic Crystals/Metamaterials, Phonon Transport, Topological Phononics, Tucson, AZ (6/2019)
- Boechler, N., “Materials with tailorable microstructure-enabled non-linear constitutive laws and their self-assembled counterparts”, Los Alamos National Laboratory Damage, Shock, and Characterization University Outreach Workshop, Los Alamos, NM (7/2019)

Publication: The key findings from this project were detailed in the publication attached below [Behrou, Reza, et al. "Topology optimization of nonlinear periodically microstructured materials for tailored homogenized constitutive properties." Composite Structures 266 (2021): 113729]

Topology optimization of nonlinear periodically microstructured materials for tailored homogenized constitutive properties

Reza Behrou[a,*], Maroun Abi Ghanem[a], Brianna C. Macnider[a], Vimarsh Verma[a], Ryan Alvey[a], Jinho Hong[a], Ashley F. Emery[b], Hyunsun Alicia Kim[c], Nicholas Boechler[a]

[a] *Department of Mechanical and Aerospace Engineering, University of California San Diego, La Jolla, CA, USA*
[b] *Department of Mechanical Engineering, University of Washington, Seattle, WA, USA*
[c] *Department of Structural Engineering, University of California San Diego, La Jolla, CA, USA*

Abstract

A topology optimization method is presented for the design of periodic microstructured materials with prescribed homogenized nonlinear constitutive properties over finite strain ranges. The mechanical model assumes linear elastic isotropic materials, geometric nonlinearity at finite strain, and a quasi-static response. The optimization problem is solved by a nonlinear programming method and the sensitivities computed via the adjoint method. Two-dimensional structures identified using this optimization method are additively manufactured and their uniaxial tensile strain response compared with the numerically predicted behavior. The optimization approach herein enables the design and development of lattice-like materials with prescribed nonlinear effective properties, for use in myriad potential applications, ranging from stress wave and vibration mitigation to soft robotics.

Keywords: topology optimization, nonlinear homogenization, finite strain, materials design, periodic microstructure, tailored constitutive properties

*Corresponding author: Reza Behrou (rbehrou@eng.ucsd.edu)

1. Introduction

The design of materials with tailored nonlinear properties is becoming increasingly important in materials sciences and engineering. This includes within the context of materials that exhibit constant properties over large deformation [1], novel wave tailoring behavior [2], multistability [3], and the ability to match the nonlinear properties of biological media [4]. Applications for these materials range from impact mitigation [5] to wearable electronics [6]. One of the ways this has been achieved is through the introduction of a periodic microstructure, where the structure of the repeating unit cell experiences geometric nonlinearity under finite strain [7]. However, it remains challenging to identify what structure is needed to obtain a desired effective nonlinear response.

One method for designing materials with nonlinear responses is the use of topology optimization. Topology optimization is an affordable form-finding design methodology to obtain the optimized distribution of materials within a design domain [8]. Design of structures with geometric nonlinearity via topology optimization has been successfully applied to a large class of structural problems such as stiffness design and compliant mechanisms [9–11]. Extensions to the design of periodic microstructures structures with nonlinear responses have also been recently reported [12, 13]. However, the examples of Refs. [12, 13] were obtained for simplified physical responses such as design of periodic microstructures with tensile loading assumptions in [12].

An alternative approach is the use of nonlinear homogenization techniques that can be integrated into the formulation of the topology optimization problem. For the case of linear homogenization techniques, this approach has been successfully used for multiscale design optimization of structures with linear responses [14]. Under the assumption of finite strain theory, nonlinear homogenization techniques [15, 16] have also been successfully integrated into topology optimization algorithms [17, 18]. However, these methods involved simplifying assumptions. In Ref. [17], unit strains were assumed at the microstructure level, which mitigates the ability for a single structure to match tailored non-

linear load-displacement behavior. In Ref. [18], the method was limited to longitudinal loading conditions.

This paper presents a topology optimization method for the design of periodic microstructured materials for tailored nonlinear homogenized constitutive responses over finite strain ranges, where the effects of macroscopically varying local strains and/or stresses are considered on the response of the periodic unit cell. The strain/stress-driven nonlinear homogenization technique are considered, following the approach given by [19]. The gradient-based topology optimization problem is formulated and the sensitivity equations are derived, allowing the design of nonlinear microstructured materials with tailored physical properties. The formulated topology optimization problem and the sensitivities are generalized for both material and geometric nonlinearities, considering the effects of macroscopically varying local strains and/or stresses on the response of Representative Volume Element (RVE). Altough the developed framework can be easily used for designing microstructures with material nonlinearity, e.g., hyperelastic and/or anisotropic materials, or design with imposed macroscale stresses, we only focus on the design of microstructured materials considering geometric nonlinearity under applied macroscale strains. The geometrically nonlinear behavior of microstructured RVE is computed using total Lagrangian finite element formulation and the linearized forward finite element problem is solved by the arc-length method [20]. The effects of macroscale deformation and loading, i.e., applied macroscopic strain and stress, on the RVE are considered through the Periodic Boundary Conditions (PBCs). To alleviate numerical instabilities for an excessive deformation caused by low-density elements, a threshold on the elemental density, i.e., void region, is applied [21]. The optimization problem is solved by a nonlinear programming method using the Method of Moving Asymptotes (MMA) optimizer [22]. The Solid Isotropic Material with Penalization (SIMP) approach [23] is used to interpolate material properties and the projection method [24] is used to regularize the optimization problem and converge to binary solutions (e.g., only one material is used in the structure, and each element is either material or void). Adjoint-based

sensitivities are developed that derives the sensitivities of the nonlinear homogenized tangent stiffness tensor with respect to both state and design variables. Two-dimensional design examples and experimental calibrations are presented to study the performance of the presented approach and the response of topology optimized designs with tailored constitutive properties.

2. Physical modeling

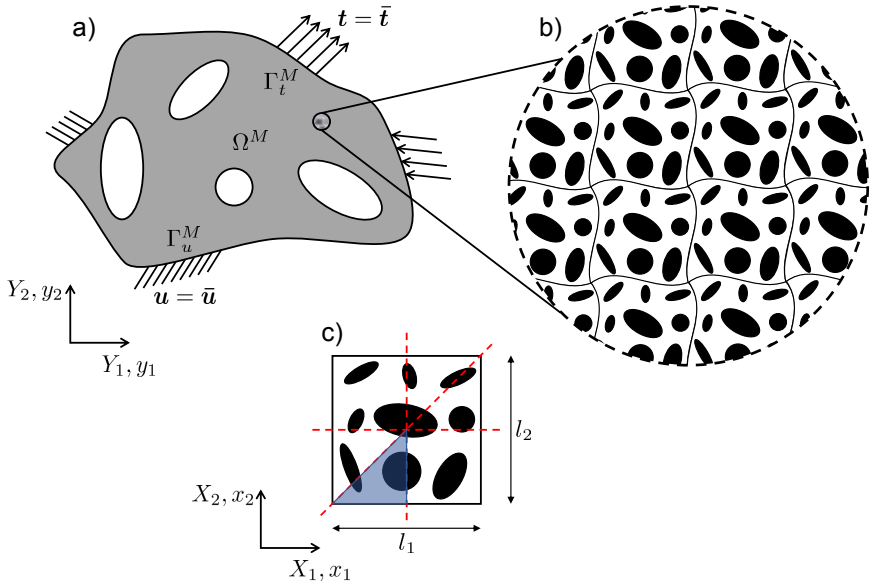

Figure 1. a) Schematic representation of a 2D macroscale Boundary Value Problem (BVP) with a material point. $\bar{\boldsymbol{u}}$ and $\bar{\boldsymbol{t}}$ are the prescribed displacement and traction, applied on the macroscale boundaries Γ_u^M and Γ_t^M, respectively, b) A periodically patterned microscale BVP at the material point, and c) Repeating Unit Cell (RUC) at the microscale. The dashed lines represent the axes of symmetry and the shaded area is the design domain.

2.1. Macro- and microscale problems

Consider macro- and microscale Boundary Value Problems (BVPs) given in Fig. 1. At both macro- and microscales, the deformation, in the absence of

body forces and accelerations, is governed by the balance of linear momentum:

$$\nabla_0^k \cdot \boldsymbol{P}^k = \boldsymbol{0}, \tag{1}$$

where $k \in \{M, \mu\}$ represents either the macroscopic entities, denoted with M, or the microscopic ones, denoted with μ, $\boldsymbol{P}$ is the first Piola-Kirchhoff stress tensor, and ∇_0 is the gradient operator with respect to the reference configuration. For the macroscale BVP, a constitutive relationship between stress and kinematic quantities can be developed through computational homogenization techniques that numerically extract the detailed computational response of a RVE at the microscopic scale [15, 16]. At any macroscopic material points, a periodically patterned RVE, given in Fig. 1b, can be considered to extract the constitutive responses through the computational homogenization [25].

2.2. Macro- and microscale kinematics

Consider the Repeating Unit Cell (RUC), given in Fig. 1c, that undergoes deformation. At both macro- and microscales, the deformation gradient, $\boldsymbol{F}$, the displacement of a material point, $\boldsymbol{u}$, and the displacement gradient, $\boldsymbol{G}$, are defined as follows:

$$\boldsymbol{F} = \frac{\partial \boldsymbol{x}}{\partial \boldsymbol{X}}, \qquad \boldsymbol{u} = \boldsymbol{x} - \boldsymbol{X}, \qquad \boldsymbol{G} = \frac{\partial \boldsymbol{u}}{\partial \boldsymbol{X}} = \boldsymbol{F} - \boldsymbol{I}, \tag{2}$$

where $\boldsymbol{x}$ and $\boldsymbol{X}$ are the coordinates of material points in the current and reference configurations, respectively, and $\boldsymbol{I}$ is the second order identity tensor. Herein we follow the approach given in [19], where the deformation of the RUC is decomposed into deformations caused by the macroscopic deformation and microscopic fluctuation displacement, as depicted in Fig. 2.

For a periodically patterned RVE, the classical first-order homogenization theory can be used to relate the macroscopic deformation, $\boldsymbol{F}^M$, to the microscopic one, $\boldsymbol{F}^\mu$, [26]:

$$\boldsymbol{F}^M = \frac{1}{\left|\Omega_{\text{rve}}\right|} \int_{\Omega_{\text{rve}}} \boldsymbol{F}^\mu d\Omega, \tag{3}$$

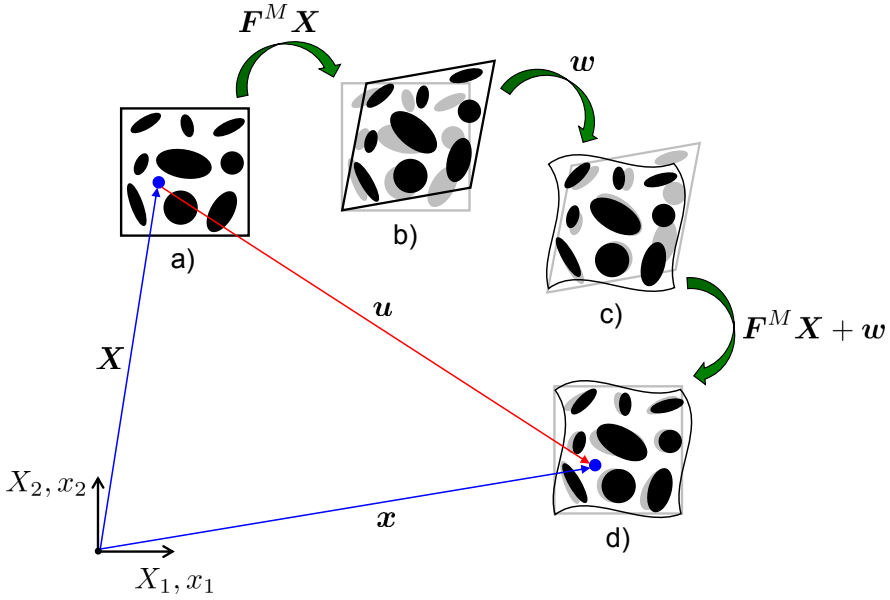

Figure 2. Schematic representation of the deformation stages in the RUC: a) reference configuration, b) the deformation caused by the macroscopic deformation gradient ($\boldsymbol{F}^M\boldsymbol{X}$), c) the microscopic fluctuation displacement ($\boldsymbol{w}$), and d) current configuration.

where Ω_{rve} is the volume of the RVE. A material point in the current configuration of the microscopic model, $\boldsymbol{x}$, can be related to the same material point in the reference configuration, $\boldsymbol{X}$, as follows [19, 26]:

$$\boldsymbol{x} = \boldsymbol{F}^M\boldsymbol{X} + \boldsymbol{w}, \tag{4}$$

where $\boldsymbol{F}^M\boldsymbol{X}$ indicates the macroscopic deformation, Fig. 2b. The macroscopic deformation gradient is constant over the RVE. The variable $\boldsymbol{w}$ indicates the displacement caused by the microscopic fluctuation, Fig. 2c.

2.3. Periodic boundary conditions

For the RVE, the relationship between the macroscopic and microscopic deformation (Eq. (3)) can be simplified to the following boundary conditions [19, 26]:

$$\frac{1}{\left|\Omega_{\text{rve}}\right|}\int_{\Gamma_{\text{rve}}} \boldsymbol{w}\cdot\boldsymbol{n}d\Gamma = \boldsymbol{0}, \tag{5}$$

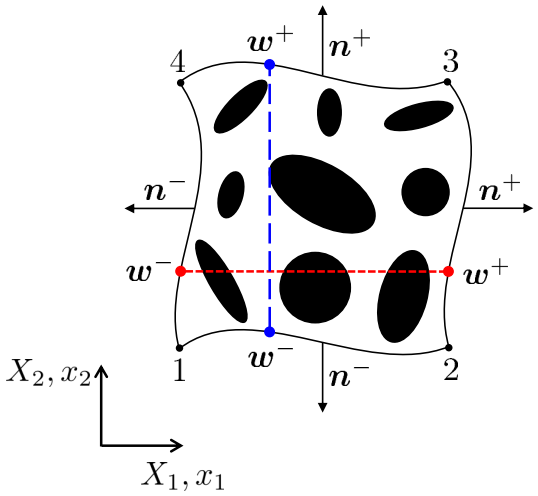

Figure 3. Schematic representation of a 2D RVE with PBCs.

where $\boldsymbol{n}$ is the outgoing normal vector over the boundaries of RVE, as shown in Fig. 3. Eq. (5) indicates that the boundary conditions on the RVE must be chosen such that the contribution of the microscale fluctuation displacement, $\boldsymbol{w}$, vanishes at the boundary. This requirement can be achieved in many ways [16]. PBCs could be an effective way to satisfy this requirement, where imposing the corresponding points on opposite boundaries (Fig. 3) yields:

$$\boldsymbol{w}^+ = \boldsymbol{w}^-. \tag{6}$$

The numerical implementation of Eq. (6) can be achieved by constructing a set of linearly independent boundary conditions, using Eqs. (2) and (4). Under the assumption of a rotation-free deformation gradient [19], the following PBCs can be used to describe an implicit relationship between the microscale displacements, $\widehat{\boldsymbol{u}}$, and the macroscale Green-Lagrange strain, $\widehat{\boldsymbol{E}}^M$ [19]:

$$\boldsymbol{T}_p\Big(\widehat{\boldsymbol{u}} - \boldsymbol{T}_X \boldsymbol{T}_s \widehat{\boldsymbol{G}}^M_{\text{sym.}}(\widehat{\boldsymbol{E}}^M)\Big) = \boldsymbol{0}, \tag{7}$$

where $\widehat{\boldsymbol{u}}$ is the microscale nodal displacement, $\widehat{\boldsymbol{G}}^M_{\text{sym.}}$ is the vector form of the symmetric displacement gradient. The matrix $\boldsymbol{T}_p$ collects all zeros, minus ones,

and ones from the PBCs of pair nodes. $\boldsymbol{T}_X$ is the matrix that contains nodal coordinates of the finite element mesh [19]. $\boldsymbol{T}_s$ is an adjustment matrix given in Appendix A. The details concerning the development of the PBCs are given in [19].

2.4. Microscale systems of equations

Following [19], a Lagrange multiplier approach can be used to formulate the homogenization problem:

$$\mathcal{L}(\widehat{\boldsymbol{u}}, \widehat{\boldsymbol{\lambda}}, \widehat{\boldsymbol{E}}^M) = \mathcal{W}^M(\widehat{\boldsymbol{u}}, \widehat{\boldsymbol{E}}^M) - \alpha \widehat{\boldsymbol{\lambda}}^T \boldsymbol{T}_p \Big(\widehat{\boldsymbol{u}} - \boldsymbol{T}_X \boldsymbol{T}_s \widehat{\boldsymbol{G}}^M_{\text{sym.}}(\widehat{\boldsymbol{E}}^M) \Big), \tag{8}$$

where $\widehat{\boldsymbol{\lambda}}$ is a vector of Lagrange multipliers, $\mathcal{W}^M$ is the macroscopic virtual work, and α is a positive numerical scaling factor [19]. The details on the derivations with respect to its variables, i.e. $\widehat{\boldsymbol{u}}$, $\widehat{\boldsymbol{\lambda}}$, $\widehat{\boldsymbol{E}}^M$, are given in [19]. These derivations result in the following systems of residual equations:

$$\boldsymbol{r}(\widehat{\boldsymbol{u}}, \widehat{\boldsymbol{\lambda}}, \widehat{\boldsymbol{E}}^M) = \begin{pmatrix} \dfrac{1}{\left|\Omega_{\text{rve}}\right|} \boldsymbol{f}_{\text{int}}(\widehat{\boldsymbol{u}}) - \alpha \boldsymbol{T}_p^T \widehat{\boldsymbol{\lambda}} \\ -\alpha \boldsymbol{T}_p \widehat{\boldsymbol{u}} + \alpha \boldsymbol{T}_p \boldsymbol{T}_X \boldsymbol{T}_s \widehat{\boldsymbol{G}}^M_{\text{sym.}}(\widehat{\boldsymbol{E}}^M) \\ \widehat{\boldsymbol{S}}^M_{\text{int}}(\widehat{\boldsymbol{\lambda}}, \widehat{\boldsymbol{E}}^M) \end{pmatrix} - \begin{pmatrix} \boldsymbol{0} \\ \boldsymbol{0} \\ \widehat{\boldsymbol{S}}^M \end{pmatrix}, \tag{9}$$

where $\boldsymbol{f}_{\text{int}}$ is the microscopic internal force vector, $\widehat{\boldsymbol{S}}^M$ is the macroscopic stress at a material point, and $\widehat{\boldsymbol{S}}^M_{\text{int}}$ is the so-called internal macroscopic stress:

$$\widehat{\boldsymbol{S}}^M_{\text{int}}(\widehat{\boldsymbol{\lambda}}, \widehat{\boldsymbol{E}}^M) = \alpha(\boldsymbol{Z}(\widehat{\boldsymbol{E}}^M))^T \widehat{\boldsymbol{\lambda}}, \quad \boldsymbol{Z} = \boldsymbol{T}_p \boldsymbol{T}_X \boldsymbol{T}_s \bar{\boldsymbol{M}}^{-1}, \quad \bar{\boldsymbol{M}} = \bar{\boldsymbol{I}} + \bar{\boldsymbol{G}}^M. \tag{10}$$

The matrix $\bar{\boldsymbol{G}}^M$ collects the components of the symmetric displacement gradient [19]. Detail on $\bar{\boldsymbol{G}}^M$ and $\bar{\boldsymbol{I}}$ is given in Appendix A.

2.5. Homogenized tangent stiffness tensor

The macroscopic tangent stiffness tensor can be defined through the stress-strain relationship. The variation of the macroscopic second Piola-Kirchhoff stress gives:

$$\delta \widehat{\boldsymbol{S}}^M = \mathbb{C}^{\text{eff}} \delta \widehat{\boldsymbol{E}}^M, \tag{11}$$

where $\mathbb{C}^{\text{eff}}$ is the homogenized tangent stiffness tensor that can be directly obtained from the converged solutions of the microscopic equilibrium equations (Eq. (9)). Following the derivations given in [19], we present a simplified homogenized tangent stiffness tensor as follows:

$$\mathbb{C}^{\text{eff}} = \mathbb{C}^{\text{s}} - \boldsymbol{Z}^T \boldsymbol{\Psi}^{-1} \boldsymbol{Z}, \qquad \boldsymbol{\Psi} = -\left|\Omega_{\text{rve}}\right| \boldsymbol{T}_p \boldsymbol{K}^{-1} \boldsymbol{T}_p^T, \tag{12}$$

where $\boldsymbol{K} = \partial \boldsymbol{f}_{\text{int}}^{\mu}(\widehat{\boldsymbol{u}})/\partial \widehat{\boldsymbol{u}}$ is the microscale tangent stiffness matrix and $\mathbb{C}^{\text{s}}$ is a type of geometrical stiffness tensor given as:

$$\mathbb{C}^{\text{s}} = -\bar{\boldsymbol{M}}^{-1} \bar{\boldsymbol{S}}^{M} \bar{\boldsymbol{M}}^{-1}, \tag{13}$$

with $\bar{\boldsymbol{S}}^{M}$ derived from the components of the internal macroscopic second Piola-Kirchhoff stress defined in Eq. (10), see Appendix A. Additional detail on the original derivation of the homogenized tangent stiffness tensor can be found [19]. We note that the presented simplified tangent stiffness tensor (Eq. (12)) facilitates the complex derivations of $\mathbb{C}^{\text{eff}}$ used for sensitivity analysis purposes, see Section 3. Detail on the simplification is given in Appendix B.

3. Sensitivity Analysis

3.1. Adjoint Sensitivity

Adjoint sensitivity analysis is used to compute the sensitivity of the objective and constraints with respect to a design variable, ϕ_k, as follows:

$$\frac{d\mathcal{Z}}{d\phi_k} = \frac{\partial \mathcal{Z}}{\partial \phi_k} + \tilde{\boldsymbol{\chi}}^T \frac{\partial \boldsymbol{r}}{\partial \phi_k}, \tag{14}$$

where $\mathcal{Z}$ is a criterion, the objective or a constraint, and $\tilde{\boldsymbol{\chi}}$ is the vector of adjoint solutions, computed by solving the following adjoint problem:

$$\left(\frac{\partial \boldsymbol{r}}{\partial \boldsymbol{s}}\right)^T \tilde{\boldsymbol{\chi}} = -\left(\frac{\partial \mathcal{Z}}{\partial \boldsymbol{s}}\right)^T. \tag{15}$$

The derivatives of the residuals with respect to state variables are computed using Eq. (9). For a generalized optimization problem, a criterion could be an

explicit function of the homogenized tangent stiffness tensor, $\mathbb{C}^{\text{eff}}$. Hence, the detail on the derivations of $\mathbb{C}^{\text{eff}}$ with respect to design and state variables are given below.

3.2. Derivative of $\mathbb{C}^{\text{eff}}$ with respect to elemental density

The partial derivative of $\mathbb{C}^{\text{eff}}$ with respect to ρ^e is given as follows:

$$\frac{\partial \mathbb{C}^{\text{eff}}}{\partial \rho^e} = \boldsymbol{Z}^T \boldsymbol{\Psi}^{-1} \frac{\partial \boldsymbol{\Psi}}{\partial \rho^e} \boldsymbol{\Psi}^{-1} \boldsymbol{Z}, \qquad \frac{\partial \boldsymbol{\Psi}}{\partial \rho^e} = \left|\Omega_{\text{rve}}\right| \boldsymbol{T}_p \boldsymbol{K}^{-1} \frac{\partial \boldsymbol{K}}{\partial \rho^e} \boldsymbol{K}^{-1} \boldsymbol{T}_p^T. \tag{16}$$

The term $\partial \boldsymbol{K}/\partial \rho^e$ can be computed from the material interpolation scheme given in Section 4.2.

3.3. Derivative of $\mathbb{C}^{\text{eff}}$ with respect to microscale displacements

The partial derivative of $\mathbb{C}^{\text{eff}}$ with respect to a displacement Degree-Of-Freedom (DOF), $\widehat{u}_p$, is given as follows:

$$\frac{\partial \mathbb{C}^{\text{eff}}}{\partial \widehat{u}_p} = \boldsymbol{Z}^T \boldsymbol{\Psi}^{-1} \frac{\partial \boldsymbol{\Psi}}{\partial \widehat{u}_p} \boldsymbol{\Psi}^{-1} \boldsymbol{Z}, \qquad \frac{\partial \boldsymbol{\Psi}}{\partial \widehat{u}_p} = \left|\Omega_{\text{rve}}\right| \boldsymbol{T}_p \boldsymbol{K}^{-1} \frac{\partial \boldsymbol{K}}{\partial \widehat{u}_p} \boldsymbol{K}^{-1} \boldsymbol{T}_p^T. \tag{17}$$

The detail on the first and second derivatives of the microscale internal strain energy is given in Appendix C. The derivations consider both material and geometric nonlinearities.

3.4. Derivative of $\mathbb{C}^{\text{eff}}$ with respect to Lagrange multipliers

The derivative of $\mathbb{C}^{\text{eff}}$ with respect to a Lagrange multiplier DOF, $\widehat{\lambda}_r$, is given as:

$$\frac{\partial \mathbb{C}^{\text{eff}}}{\partial \widehat{\lambda}_r} = -\bar{\boldsymbol{M}}^{-1} \frac{\partial \bar{\boldsymbol{S}}^M}{\partial \widehat{\boldsymbol{S}}^M_{\text{int}}} \frac{\partial \widehat{\boldsymbol{S}}^M_{\text{int}}}{\partial \lambda_r} \bar{\boldsymbol{M}}^{-1}. \tag{18}$$

The term $\partial \widehat{\boldsymbol{S}}^M_{\text{int}}/\partial \lambda_r$ can be computed from Eq. (10) and the derivatives of $\bar{\boldsymbol{S}}^M$ with respect to internal stress components can be computed from Eq. (A.5).

3.5. Derivative of $\mathbb{C}^{\text{eff}}$ with respect to macroscale strains

The derivative of $\mathbb{C}^{\text{eff}}$ with respect to a macroscale strain DOF, $\widehat{E}_r^M$, can be computed as follows:

$$\frac{\partial \mathbb{C}^{\text{eff}}}{\partial \widehat{E}_r^M} = \frac{\partial \mathbb{C}^{\text{s}}}{\partial \widehat{E}_r^M} - \Big(\frac{\partial \boldsymbol{Z}^T}{\partial \widehat{E}_r^M} \boldsymbol{\Psi}^{-1} \boldsymbol{Z} + \boldsymbol{Z}^T \boldsymbol{\Psi}^{-1} \frac{\partial \boldsymbol{Z}}{\partial \widehat{E}_r^M} \Big), \tag{19}$$

where

$$\begin{aligned} \frac{\partial \mathbb{C}^{\text{s}}}{\partial \widehat{E}_r^M} &= -\left(\frac{\partial \bar{\boldsymbol{M}}^{-1}}{\partial \widehat{E}_r^M} \bar{\boldsymbol{S}}^M \bar{\boldsymbol{M}}^{-1} + \bar{\boldsymbol{M}}^{-1} \frac{\partial \bar{\boldsymbol{S}}^M}{\partial \widehat{E}_r^M} \bar{\boldsymbol{M}}^{-1} + \bar{\boldsymbol{M}}^{-1} \bar{\boldsymbol{S}}^M \frac{\partial \bar{\boldsymbol{M}}^{-1}}{\partial \widehat{E}_r^M} \right), \\ \frac{\partial \boldsymbol{Z}}{\partial \widehat{E}_r^M} &= -\boldsymbol{Z} \frac{\partial \bar{\boldsymbol{G}}^M}{\partial \widehat{\boldsymbol{G}}^M_{\text{sym.}}} \bar{\boldsymbol{M}}^{-1} \bar{\boldsymbol{M}}^{-1}, \end{aligned} \tag{20}$$

with

$$\frac{\partial \bar{\boldsymbol{M}}^{-1}}{\partial \widehat{E}_r^M} = -\bar{\boldsymbol{M}}^{-1} \frac{\partial \bar{\boldsymbol{G}}^M}{\partial \widehat{\boldsymbol{G}}^M_{\text{sym.}}} \bar{\boldsymbol{M}}^{-1} \bar{\boldsymbol{M}}^{-1}. \tag{21}$$

The derivatives of $\bar{\boldsymbol{G}}^M$ with respect to the components of $\widehat{\boldsymbol{G}}^M_{\text{sym.}}$ can be computed from Eq. (A.3).

4. Topology Optimization

The optimization problem presented here is included as an example of how to consider the components of the homogenized tangent stiffness tensor, $\mathbb{C}^{\text{eff}}$, in the formulation of the objective function and constraints. Although many combinations of individual components of the homogenized tangent stiffness tensor can be considered (for instance, to maximize the material bulk modulus [27, 28] or Poisson's ratio [29]) in this paper, the objective is defined as to minimize the difference between the computed and target tangent stiffness tensor. The generalized formulation of the objective and constraints, material interpolation, and regularization are discussed below.

4.1. Objective and Constraints

The optimization problem for minimizing the difference between the homogenized tangent stiffness tensor, $\mathbb{C}^{\text{eff}}$, and the target tangent stiffness tensor,

$\mathbb{C}^{\text{target}}$, is formulated as follows:

$$\begin{aligned} \min_{\boldsymbol{\phi}} \quad & z = \sum_{i,j,k,l=1}^{D} \bar{w}_{ijkl}\Big(\mathbb{C}^{\text{eff}}_{ijkl}(\boldsymbol{s}(\boldsymbol{\phi}),\boldsymbol{\phi}) - \mathbb{C}^{\text{target}}_{ijkl}\Big)^2 \\ \text{subject to} \quad & \begin{cases} \boldsymbol{r}(\boldsymbol{s}(\boldsymbol{\phi}),\boldsymbol{\phi}) = \boldsymbol{0} \\ \sum_{e\in\Omega_{\text{rve}}} \rho^e(\boldsymbol{\phi}) v^e \le V_{max} \\ 0 \le \phi_k \le 1 \qquad \forall k = 1,...,N_\phi \end{cases} \end{aligned}, \tag{22}$$

where z is the objective, D is the spatial dimension, $\bar{w}$ is the weighting factor, $\boldsymbol{\phi}$ is the vector of independent design variables, ρ^e is the fictitious elemental density, v^e is the elemental volume, V_{max} is the prescribed volume fraction of the solid material, and $\boldsymbol{s} = [\widehat{\boldsymbol{u}}, \widehat{\boldsymbol{\lambda}}, \widehat{\boldsymbol{E}}^M]^T$ is the vector of state variables satisfying the discretized microscale residual equations, i.e., $\boldsymbol{r}(\boldsymbol{s}(\boldsymbol{\phi}),\boldsymbol{\phi}) = \boldsymbol{0}$. At each design iteration, the Nested ANalysis and Design (NAND) approach is used to solve the microscale finite element problem. The independent design variables are bounded with lower and upper bounds with N_ϕ that denotes the number of design variables.

4.2. Material Interpolation

The SIMP approach [23] is used to interpolate material properties with an artificial power law that penalizes intermediate density values. Using this approach, the stiffness of the microstructure is related to topology through the Young's modulus of an element. Within the microscopic domain, the Young's modulus is defined as a function of elemental density, ρ^e, as follows:

$$E^e(\rho^e) = \Big(\rho^e_{min} + (\rho^e)^{\bar{p}}\big(1 - \rho^e_{min}\big)\Big)E^e_0, \tag{23}$$

where E^e_0 is the Young's modulus of pure solid material, $\bar{p} \ge 1$ is the SIMP exponent penalty term, and ρ^e_{min} is a small positive number to maintain positive definiteness of the global stiffness matrix. We set $\rho^e = 1$ for the solid region and $\rho^e = 0$ for the void region.

4.3. Regularization

To circumvent instabilities, caused by checkerboard patterns and mesh dependent designs [30], and convergence to binary solutions, numerical regularization approaches such as filtering [10] and projection [24, 31, 32] can be used. In this paper, we adopt the linear density filtering [10] and the threshold projection [24] approaches. Using the linear filtering plus–projection, the independent nodal design variables field, $\boldsymbol{\phi}$, is first mapped onto an element-wise constant filtered field, $\mu^e(\boldsymbol{\phi})$, using the following linear filtering scheme:

$$\mu^e(\boldsymbol{\phi}) = \frac{\sum\limits_{i \in N^e} \hat{w}_i \phi_i}{\sum\limits_{i \in N^e} \hat{w}_i}, \quad \text{with} \quad \hat{w}_i = \frac{r_{min} - \parallel x_i - x^e \parallel}{r_{min}}, \tag{24}$$

where N^e defines set containing all design variables located within a radius r_{min} of the centroid of e, x_i is the position of node i, and x^e is the central position of element e. The elemental density is then related to the filtered design variables through the threshold projection:

$$\rho^e(\boldsymbol{\phi}) = \frac{\tanh(\beta\eta) + \tanh(\beta(\mu^e(\boldsymbol{\phi}) - \eta))}{\tanh(\beta\eta) + \tanh(\beta(1 - \eta))}, \tag{25}$$

where η is the threshold of the projection and $\beta > 0$ dictates the curvature of the regularization which approaches the Heaviside function as $\beta \to \infty$ [24].

5. Algorithmic Summary

For the design problems presented in this paper, the MMA optimizer [22] is used to solve the optimization problem. The most relevant MMA parameters are summarized in Table 1. At each design iteration, the microscale nonlinear finite element problem is solved using the arc-length method [20]. The finite element problem of the linearized system is considered converged if the relative residuals are less than 10^{-10}. The solution for the adjoint variables is obtained using the direct linear solver [33]. To ensure smooth evolution in the design and avoid oscillation in the design history and convergence to undesirable local minima continuations on the β parameter (Eq. (25)) are considered [24].

Table 1. MMA parameters used in topology optimization problems.

Description	Symbol	Value
initial asymptote parameter	σ_{MMA}	0.017
lower asymptote adaptivity	α_-	0.55
upper asymptote adaptivity	α_+	1.05
constraint penalty	c_i	1000

The optimization problem is considered converged if the relative change of the objective function is less than 10^{-6} and all constraints are satisfied.

6. Numerical examples

In this section, we implement the topology optimization approach in 2D, assuming plane stress state, for uniaxial applied strain. For all numerical examples, the periodic microstructured RVE given in Fig. 1c is considered, where $l_1 = l_2 = 1$. The domain is discretized with 100×100 bilinear quadrilateral elements. We note that our mesh refinement studies show negligible discretization errors. Symmetry on the design is enforced in the axial directions and along the diagonals (Fig. 1c). To eliminate the rigid-body translation, an arbitrary node in the solid region of the design domain (shaded area in Fig. 1c) of the microscale problem is constrained in all directions and reflected based on the applied axes of symmetry. The base material parameters are set to $E = 1$ and $\nu = 0.3$.

6.1. Topology optimized designs

In the section, we present an example using this optimization framework where we start with two different initial guesses, and seek to match the response of an arbitrary target geometry, i.e., $\mathbb{C}^{\text{target}}$ at 20% strain, as shown in Fig. 4a. Table 2 summarizes the finite element and design parameters defining the optimization problem. The minimum desirable features are set equal to the minimum feature of the target shape through the filter radius given in Table 2.

Table 2. Finite element and optimization parameters for the design problems.

Description	Symbol	Value
applied macroscale strain	$\widehat{E}^M_{yy}$	20%
RVE thickness	–	0.3
target volume fraction	V_{max}	0.305
filter radius	r_{min}	0.0875
SIMP exponent	$\bar{p}$	3
small positive number	ρ^e_{min}	10^{-4}
threshold of the projection	η	0.50
curvature of regularization	β	$2 \leq \beta \leq 100$

The resulting optimized microstructures are shown in Fig. 4c and Fig. 4e. The results reveal the influence of the initial guess on the response of the topology optimization designs. For all designs, the responses of the target shape ($\mathbb{C}^{\text{target}}$) are achieved, satisfying the prescribed volume constraint, i.e., solid materials in the target shape. The evolution of the objective functions is shown in Fig. 4f. The reported maximum discrepancy between the optimized and the target responses is less than 0.9%. The oscillations in the objectives are caused by the continuation in the projection parameter. Although the topology optimized designs qualitatively match the physical response of the target shape, the results reveal that the optimized design is not unique and for the same physical response multiple optimized designs can be obtained.

6.2. Experimental calibration

To experimentally evaluate the performance of the optimized design, the target geometry and the optimized design given in Fig. 4c were fabricated and tested. The samples were 3D printed using a Connex3 Objet350 printer and FLX9785 material. Each 3D printed sample was glued to acrylic plates along the top and bottom edges in order to ensure better tester gripping. Under the uniaxial loading conditions, the mechanical testing of each sample was perfor-

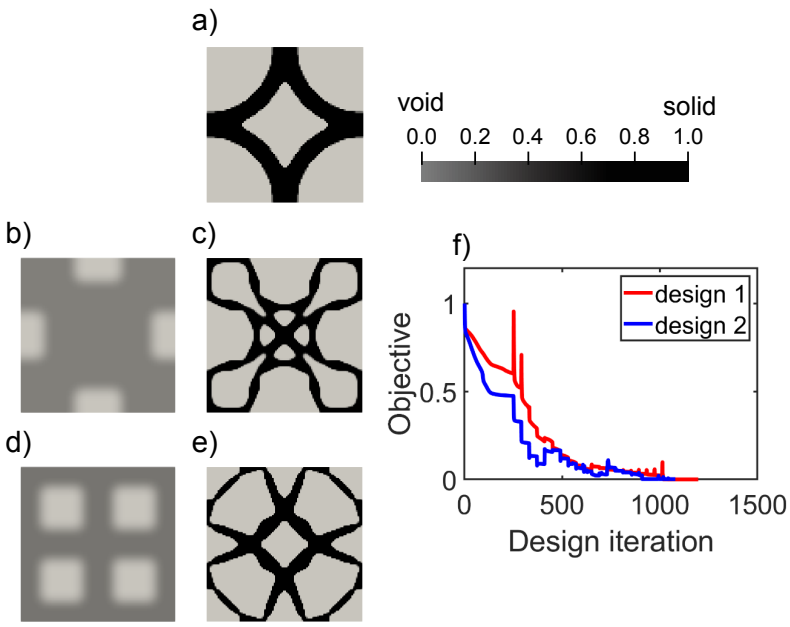

Figure 4. a) The target geometry used in topology optimization problems. b) Initial guess for design 1. c) Optimized design for design 1. d) Initial guess for design 2. e) Optimized design for design 2. f) The objective history for design 1 and 2.

med on an Instron 5965 tester. Tension tests were performed at a rate of 0.1 mm/second.

The deformed configurations of the numerical and experimental samples are shown in Fig. 5a and Fig. 5f. The comparison on the experimental and numerical stress-strain responses is shown in Fig. 6. The results show qualitatively similar trends in the stress-strain responses. However, the use of elastomeric type materials, and thus nonlinear elastic material response, in the experimental samples could be the possible cause of the discrepancy between the experimental and numerical results. For both designs 1 and 2, it is clear that the numerical responses cross the target response at 20% strain. For design 1, the experimental response crosses the target response close to 20% applied strain, as intended.

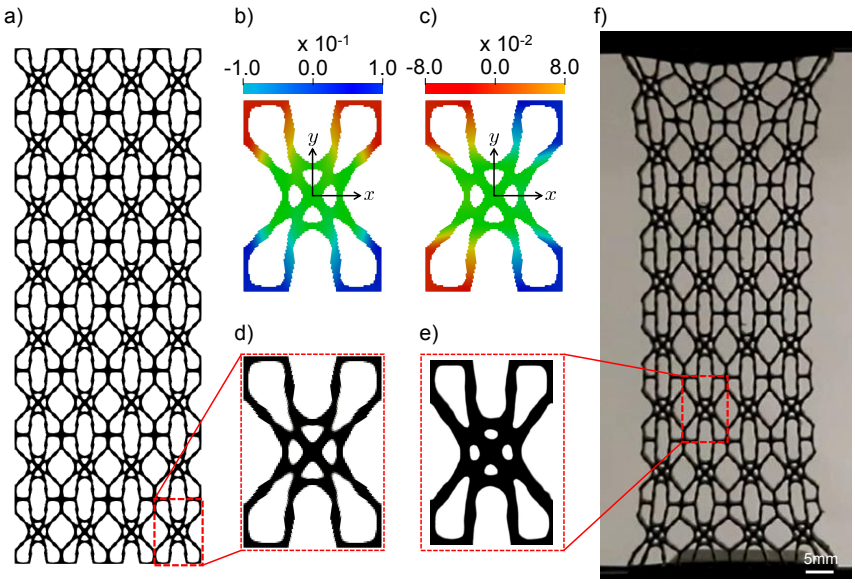

Figure 5. The numerical and experimental deformed configurations of the optimized microstructure given in Fig. 4c at $\widehat{E}^M_{yy} = 20\%$, a) the deformed 4×8 microstructured lattice – simulation; b) displacement in y direction – simulation; c) displacement in x direction – simulation; d) the deformed RVE – simulation; e) the deformed RVE – experiment (background color removed thorough the image processing); and f) the deformed 4×8 microstructured lattice – experiment.

7. Conclusions

This paper presented a method for the design optimization of periodic microstructured materials with prescribed nonlinear constitutive properties over finite strain ranges. For the demonstrated examples, we considered only the geometric nonlinearity. A optimization problems were formulated to match the mechanical response of an arbitrary target geometry. This was accomplished by integrating a nonlinear homogenization technique, following [19], into the formulation of a topology optimization algorithm that considers the effects of locally varying macroscopic strain/stress on the response of microsctructured unit cell. Adjoint sensitivities were derived to computed the generalized sensitivities of the homogenized tangent stiffness tensor with respect to design and

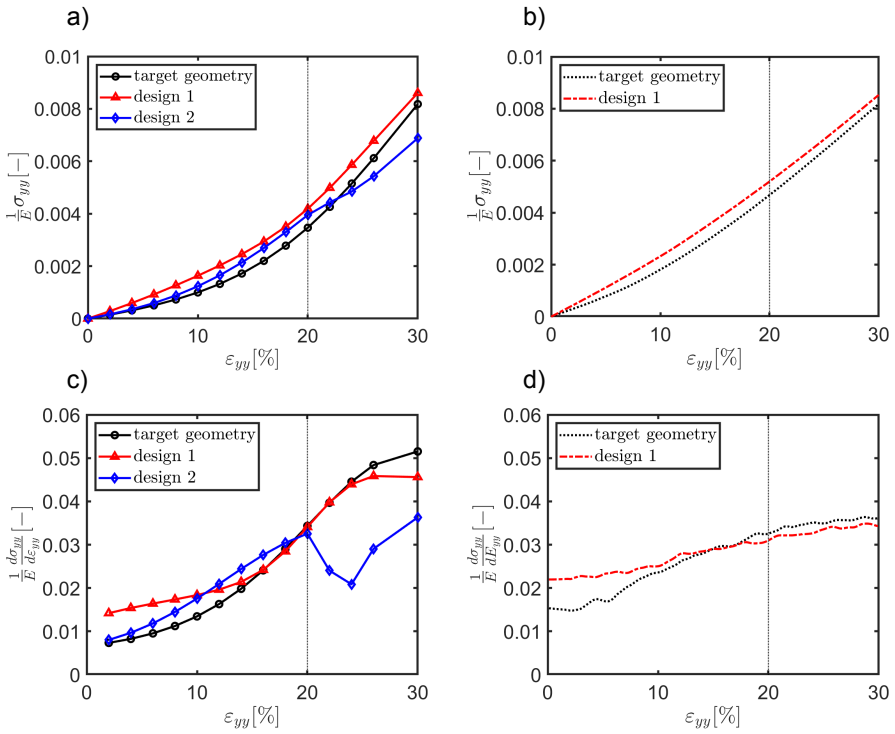

Figure 6. a) The numerical stress-strain responses for the target geometry and optimized designs. b) The experimental stress-strain responses for the target geometry and design 1. c) The derivative of the numerical stress-strain responses with respect to the strain in loading direction (ε_{yy}). d) The derivative of the experimental stress-strain responses with respect to the strain in loading direction (ε_{yy}).

state variables. Two-dimensional topology optimization examples were considered to study the performance of the presented approach. An optimized design was additively manufactured and its response was calibrated through the experiment. The topology optimization approach enables design of 2D and 3D nonlinear lattice-like materials with tailored homogenized constitutive properties, for applications ranging from impact mitigation to wearable electronics.

Acknowledgments

This work was supported by the Air Force Office of Scientific Research under award number FA9550-16-1-0142. R. B. thanks Dr. N. P. van Dijk for useful discussions on the homogenization technique.

References

[1] A. Clausen, F. Wang, J. S. Jensen, O. Sigmund, J. A. Lewis, Topology optimized architectures with programmable poisson's ratio over large deformations, Advanced Materials 27 (37) (2015) 5523–5527.

[2] M. I. Hussein, M. J. Leamy, M. Ruzzene, Dynamics of phononic materials and structures: Historical origins, recent progress, and future outlook, Applied Mechanics Reviews 66 (4) (2014) 040802.

[3] S. Shan, S. H. Kang, J. R. Raney, P. Wang, L. Fang, F. Candido, J. A. Lewis, K. Bertoldi, Multistable architected materials for trapping elastic strain energy, Advanced Materials 27 (29) (2015) 4296–4301.

[4] Q. Ma, H. Cheng, K.-I. Jang, H. Luan, K.-C. Hwang, J. A. Rogers, Y. Huang, Y. Zhang, A nonlinear mechanics model of bio-inspired hierarchical lattice materials consisting of horseshoe microstructures, Journal of the Mechanics and Physics of Solids 90 (2016) 179–202.

[5] H. Yasuda, Y. Miyazawa, E. G. Charalampidis, C. Chong, P. G. Kevrekidis, J. Yang, Origami-based impact mitigation via rarefaction solitary wave creation, Science advances 5 (5) (2019) eaau2835.

[6] J. A. Rogers, T. Someya, Y. Huang, Materials and mechanics for stretchable electronics, science 327 (5973) (2010) 1603–1607.

[7] V. Nesterenko, Dynamics of heterogeneous materials, Springer Science & Business Media, 2013.

[8] M. P. Bendsøe, N. Kikuchi, Generating optimal topologies in structural design using a homogenization method, Computer methods in applied mechanics and engineering 71 (2) (1988) 197–224.

[9] T. Buhl, C. B. Pedersen, O. Sigmund, Stiffness design of geometrically nonlinear structures using topology optimization, Structural and Multidisciplinary Optimization 19 (2) (2000) 93–104.

[10] T. E. Bruns, D. A. Tortorelli, Topology optimization of non-linear elastic structures and compliant mechanisms, Computer methods in applied mechanics and engineering 190 (26-27) (2001) 3443–3459.

[11] H. C. Gea, J. Luo, Topology optimization of structures with geometrical nonlinearities, Computers & Structures 79 (20-21) (2001) 1977–1985.

[12] F. Wang, O. Sigmund, J. S. Jensen, Design of materials with prescribed nonlinear properties, Journal of the Mechanics and Physics of Solids 69 (2014) 156–174.

[13] K. L. Manktelow, M. J. Leamy, M. Ruzzene, Topology design and optimization of nonlinear periodic materials, Journal of the Mechanics and Physics of Solids 61 (12) (2013) 2433–2453.

[14] L. Xia, P. Breitkopf, Recent advances on topology optimization of multiscale nonlinear structures, Archives of Computational Methods in Engineering 24 (2) (2017) 227–249.

[15] M. G. Geers, V. G. Kouznetsova, W. Brekelmans, Multi-scale computational homogenization: Trends and challenges, Journal of computational and applied mathematics 234 (7) (2010) 2175–2182.

[16] M. G. Geers, V. G. Kouznetsova, K. Matouš, J. Yvonnet, Homogenization methods and multiscale modeling: Nonlinear problems, Encyclopedia of Computational Mechanics Second Edition (2017) 1–34.

[17] P. B. Nakshatrala, D. A. Tortorelli, K. Nakshatrala, Nonlinear structural design using multiscale topology optimization. part i: Static formulation, Computer Methods in Applied Mechanics and Engineering 261 (2013) 167–176.

[18] D. Kumar, Z.-P. Wang, L. H. Poh, S. T. Quek, Isogeometric shape optimization of smoothed petal auxetics with prescribed nonlinear deformation, Computer Methods in Applied Mechanics and Engineering 356 (2019) 16–43.

[19] N. P. van Dijk, Formulation and implementation of stress-driven and/or strain-driven computational homogenization for finite strain, International Journal for Numerical Methods in Engineering 107 (12) (2016) 1009–1028.

[20] R. De Borst, M. A. Crisfield, J. J. Remmers, C. V. Verhoosel, Nonlinear finite element analysis of solids and structures, John Wiley & Sons, 2012.

[21] R. Behrou, R. Ranjan, J. K. Guest, Adaptive topology optimization for incompressible laminar flow problems with mass flow constraints, Computer Methods in Applied Mechanics and Engineering 346 (2019) 612–641.

[22] K. Svanberg, The method of moving asymptotes—a new method for structural optimization, International journal for numerical methods in engineering 24 (2) (1987) 359–373.

[23] M. P. Bendsøe, Optimal shape design as a material distribution problem, Structural and Multidisciplinary Optimization 1 (4) (1989) 193–202.

[24] F. Wang, B. S. Lazarov, O. Sigmund, On projection methods, convergence and robust formulations in topology optimization, Structural and Multidisciplinary Optimization 43 (6) (2011) 767–784.

[25] J. Guedes, N. Kikuchi, Preprocessing and postprocessing for materials based on the homogenization method with adaptive finite element methods, Computer methods in applied mechanics and engineering 83 (2) (1990) 143–198.

[26] V. Kouznetsova, W. Brekelmans, F. Baaijens, An approach to micro-macro modeling of heterogeneous materials, Computational mechanics 27 (1) (2001) 37–48.

[27] O. Sigmund, A new class of extremal composites, Journal of the Mechanics and Physics of Solids 48 (2) (2000) 397–428.

[28] S. Amstutz, S. Giusti, A. Novotny, E. de Souza Neto, Topological derivative for multi-scale linear elasticity models applied to the synthesis of microstructures, International Journal for Numerical Methods in Engineering 84 (6) (2010) 733–756.

[29] E. Andreassen, B. S. Lazarov, O. Sigmund, Design of manufacturable 3d extremal elastic microstructure, Mechanics of Materials 69 (1) (2014) 1–10.

[30] O. Sigmund, J. Petersson, Numerical instabilities in topology optimization: a survey on procedures dealing with checkerboards, mesh-dependencies and local minima, Structural optimization 16 (1) (1998) 68–75.

[31] J. K. Guest, J. H. Prévost, T. Belytschko, Achieving minimum length scale in topology optimization using nodal design variables and projection functions, International journal for numerical methods in engineering 61 (2) (2004) 238–254.

[32] O. Sigmund, Morphology-based black and white filters for topology optimization, Structural and Multidisciplinary Optimization 33 (4-5) (2007) 401–424.

[33] J. R. Gilbert, C. Moler, R. Schreiber, Sparse matrices in matlab: Design and implementation, SIAM Journal on Matrix Analysis and Applications 13 (1) (1992) 333–356.

[34] T.-T. Lu, S.-H. Shiou, Inverses of 2× 2 block matrices, Computers & Mathematics with Applications 43 (1-2) (2002) 119–129.

Appendix A. Homogenization matrices

The following relationship is held between the symmetric displacement gradient vector, $\widehat{\boldsymbol{G}}^M_{\text{sym.}}$, the original displacement gradient, $\widehat{\boldsymbol{G}}^M$, and the Green-Lagrange strain tensors (under the assumption of the rotation-free deformation) [19]:

$$\begin{aligned}\widehat{\boldsymbol{G}}^M &= \boldsymbol{T}_s \widehat{\boldsymbol{G}}^M_{\text{sym.}},\\ \widehat{\boldsymbol{E}}^M &= \Big(\bar{\boldsymbol{I}} + \frac{1}{2}\bar{\boldsymbol{G}}^M\Big)\widehat{\boldsymbol{G}}^M_{\text{sym.}},\end{aligned} \tag{A.1}$$

where

$$\boldsymbol{T}_s = \begin{bmatrix} 1 & 0 & 0 & 0 & 0 & 0 & 0 & 0 & 0\\ 0 & 0 & 0 & 0 & 1 & 0 & 0 & 0 & 0\\ 0 & 0 & 0 & 0 & 0 & 0 & 0 & 0 & 1\\ 0 & 1 & 0 & 1 & 0 & 0 & 0 & 0 & 0\\ 0 & 0 & 0 & 0 & 0 & 1 & 0 & 1 & 0\\ 0 & 0 & 1 & 0 & 0 & 0 & 1 & 0 & 0 \end{bmatrix}^T, \tag{A.2}$$

The matrix $\bar{\boldsymbol{G}}^M$ collects the components of the symmetric displacement gradient, $\widehat{\boldsymbol{G}}^M_{\text{sym.}}$, is given as follows:

$$\bar{\boldsymbol{G}}^M = \begin{bmatrix} G^M_{11} & 0 & 0 & G^M_{12} & 0 & G^M_{31}\\ 0 & G^M_{22} & 0 & G^M_{12} & G^M_{23} & 0\\ 0 & 0 & G^M_{33} & 0 & G^M_{23} & G^M_{31}\\ G^M_{12} & G^M_{12} & 0 & (G^M_{11}+G^M_{22}) & G^M_{31} & G^M_{23}\\ 0 & G^M_{23} & G^M_{23} & G^M_{31} & (G^M_{22}+G^M_{33}) & G^M_{12}\\ G^M_{31} & 0 & G^M_{31} & G^M_{23} & G^M_{12} & (G^M_{33}+G^M_{11}) \end{bmatrix}. \tag{A.3}$$

The diagonal matrix, $\bar{\boldsymbol{I}}$, is defined as follows:

$$\bar{\boldsymbol{I}} = \begin{bmatrix} 1 & & & & & \\ & 1 & & & \mathbf{0} & \\ & & 1 & & & \\ & & & 2 & & \\ & \mathbf{0} & & & 2 & \\ & & & & & 2 \end{bmatrix}. \tag{A.4}$$

The so-called geometrical stress, $\bar{\boldsymbol{S}}^M$, is be derived from the components of the internal macroscopic second Piola-Kirchhoff stress, $\widehat{\boldsymbol{S}}^M_{\text{int}}$:

$$\bar{\boldsymbol{S}}^M = \begin{bmatrix} S_{11} & 0 & 0 & S_{12} & 0 & S_{31} \\ 0 & S_{22} & 0 & S_{12} & S_{23} & 0 \\ 0 & 0 & S_{33} & 0 & S_{23} & S_{31} \\ S_{12} & S_{12} & 0 & (S_{11}+S_{22}) & S_{31} & S_{23} \\ 0 & S_{23} & S_{23} & S_{31} & (S_{22}+S_{33}) & S_{12} \\ S_{31} & 0 & S_{31} & S_{23} & S_{12} & (S_{33}+S_{11}) \end{bmatrix}. \tag{A.5}$$

Appendix B. Simplified form of the homogenized stiffness tensor

The homogenized tangent stiffness tensor can be numerically computed from the converged solutions of the microscale equilibrium equations (Eq. (9)) as follows [19]:

$$\begin{aligned} \mathbb{C}^{\text{eff}}(\widehat{\boldsymbol{u}}, \widehat{\boldsymbol{\lambda}}, \widehat{\boldsymbol{E}}^M) &= \mathbb{C}^{\text{s}}(\widehat{\boldsymbol{\lambda}}, \widehat{\boldsymbol{E}}^M) \\ &- \begin{bmatrix} \boldsymbol{0} & \alpha \boldsymbol{Z}^T(\widehat{\boldsymbol{E}}^M) \end{bmatrix} \underbrace{\begin{bmatrix} \dfrac{1}{\left|\Omega_{\text{rve}}\right|}\boldsymbol{K}(\widehat{\boldsymbol{u}}) & -\alpha \boldsymbol{T}_p^T \\ -\alpha \boldsymbol{T}_p & \boldsymbol{0} \end{bmatrix}^{-1}}_{\boldsymbol{\Upsilon}} \begin{bmatrix} \boldsymbol{0} \\ \alpha \boldsymbol{Z}(\widehat{\boldsymbol{E}}^M) \end{bmatrix}, \end{aligned} \tag{B.1}$$

Eq. (B.1) can be simplified as follows. Consider a 2×2 block matrices given as follows:

$$\boldsymbol{R} = \begin{bmatrix} \boldsymbol{A}_{k\times m} & \boldsymbol{B}_{k\times n} \\ \boldsymbol{C}_{l\times m} & \boldsymbol{D}_{l\times n} \end{bmatrix}_{(k+l)\times(m+n)}, \tag{B.2}$$

where $k+l = m+n$. For the case when $\boldsymbol{A}$ is a non-singular square matrix and $k = m$ and $l = n$, the non-singular square matrix $\boldsymbol{R}$ is invertible if and only if the schur complement (i.e., $\boldsymbol{D} - \boldsymbol{C}\boldsymbol{A}^{-1}\boldsymbol{B}$) of $\boldsymbol{A}$ is invertible [34]. For this case the inverse of $\boldsymbol{R}$ is given as follows [34]:

$$\boldsymbol{R}^{-1} = \begin{bmatrix} \boldsymbol{A}^{-1} + \boldsymbol{A}^{-1}\boldsymbol{B}(\boldsymbol{D}-\boldsymbol{C}\boldsymbol{A}^{-1}\boldsymbol{B})^{-1}\boldsymbol{C}\boldsymbol{A}^{-1} & -\boldsymbol{A}^{-1}\boldsymbol{B}(\boldsymbol{D}-\boldsymbol{C}\boldsymbol{A}^{-1}\boldsymbol{B})^{-1} \\ -(\boldsymbol{D}-\boldsymbol{C}\boldsymbol{A}^{-1}\boldsymbol{B})^{-1}\boldsymbol{C}\boldsymbol{A}^{-1} & (\boldsymbol{D}-\boldsymbol{C}\boldsymbol{A}^{-1}\boldsymbol{B})^{-1} \end{bmatrix}. \tag{B.3}$$

Let's consider the matrix $\boldsymbol{\Upsilon}$ containing a 2×2 block of matrices given in Eq. (B.1). Its internal matrices have the aforementioned properties, where

$$\boldsymbol{A} = \frac{1}{\left|\Omega_{\text{rve}}\right|}\boldsymbol{K}, \quad \boldsymbol{B} = \boldsymbol{C}^T = -\alpha \boldsymbol{T}_p^T, \quad \boldsymbol{D} = \boldsymbol{0}. \tag{B.4}$$

The stiffness matrix, $\boldsymbol{K}$, is a non-singular square matrix and $k = m$ and $l = n$, therefore, $\boldsymbol{\Upsilon}^{-1} = \boldsymbol{R}^{-1}$. The use of Eqs. (B.3) and (B.4) in (B.1) yields the simplified form of the homogenized stiffness tensor given in (12).

Appendix C. Microscale internal energy and its first and second derivatives

At the microscale and in the absence of external forces, the variational form of the internal strain energy can be written as:

$$\delta \mathcal{W}_{\text{int}}^{\mu}(\widehat{\boldsymbol{u}}) = \int_{\Omega_{\text{rve}}} S_{IJ}^{\mu}(E_{IJ}^{\mu}(\widehat{\boldsymbol{u}}))\ \delta E_{IJ}^{\mu}(\widehat{\boldsymbol{u}})\ d\Omega, \tag{C.1}$$

where *boldsymbolE*$^{\mu}$ and *boldsymbolS*$^{\mu}$ is the Green-Lagrange strain and the Second Piola-Kirchhoff stress tensor, respectively. Linearization of the in internal strain energy leads to the following derivatives:

$$\frac{\partial \delta \mathcal{W}_{\text{int}}^{\mu}}{\partial \widehat{u}_m} = \int_{\Omega_{\text{rve}}} \Big(\frac{\partial \delta E_{IJ}^{\mu}}{\partial \widehat{u}_m} S_{IJ}^{\mu} + \delta E_{IJ}^{\mu} C_{IJKL}^{\mu} \frac{\partial E_{KL}^{\mu}}{\partial \widehat{u}_m} \Big)\ d\Omega. \tag{C.2}$$

And the second derivatives gives:

$$\begin{aligned} \frac{\partial}{\partial \widehat{u}_t}\Big(\frac{\partial \delta \mathcal{W}_{\text{int}}^{\mu}}{\partial \widehat{u}_m} \Big) = \int_{\Omega_{\text{rve}}} \Big(& \frac{\partial \delta E_{IJ}^{\mu}}{\partial \widehat{u}_m} C_{IJKL}^{\mu} \frac{\partial E_{KL}^{\mu}}{\partial \widehat{u}_t} + \frac{\partial \delta E_{IJ}^{\mu}}{\partial \widehat{u}_t} C_{IJKL}^{\mu} \frac{\partial E_{KL}^{\mu}}{\partial \widehat{u}_m} \\ & + \delta E_{IJ}^{\mu} \frac{\partial C_{IJKL}^{\mu}}{\partial \widehat{u}_t} \frac{\partial E_{KL}^{\mu}}{\partial \widehat{u}_m} + \delta E_{IJ}^{\mu} C_{IJKL}^{\mu} \frac{\partial}{\partial \widehat{u}_t}\Big(\frac{\partial E_{KL}^{\mu}}{\partial \widehat{u}_m} \Big) \Big)\ d\Omega. \end{aligned} \tag{C.3}$$

The microscale Green-Lagrange strain tensor and it's derivatives is expressed as:

$$E_{KL}^{\mu} = \frac{1}{2}\big((F_{Kp}^{\mu})^T F_{pL}^{\mu} - \delta_{KL} \big), \qquad F_{pL}^{\mu} = \frac{\partial u_p}{\partial X_L^{\mu}} + \delta_{pL}, \tag{C.4}$$

$$\frac{\partial E_{KL}^{\mu}}{\partial \widehat{u}_m} = \frac{1}{2}\Big(\frac{\partial (F_{Kp}^{\mu})^T}{\partial \widehat{u}_m} F_{pL}^{\mu} + (F_{Kp}^{\mu})^T \frac{\partial F_{pL}^{\mu}}{\partial \widehat{u}_m} \Big), \tag{C.5}$$

$$\delta E^{\mu}_{IJ} = \frac{1}{2}\Big(F^{\mu}_{iJ}\frac{\partial \delta u_i}{\partial X^{\mu}_I} + F^{\mu}_{iI}\frac{\partial \delta u_i}{\partial X^{\mu}_J}\Big), \tag{C.6}$$

$$\frac{\partial \delta E^{\mu}_{IJ}}{\partial \widehat{u}_m} = \frac{1}{2}\Big(\frac{\partial F^{\mu}_{iJ}}{\partial \widehat{u}_m}\frac{\partial \delta u_i}{\partial X^{\mu}_I} + \frac{\partial F^{\mu}_{iI}}{\partial \widehat{u}_m}\frac{\partial \delta u_i}{\partial X^{\mu}_J}\Big), \tag{C.7}$$

$$\frac{\partial}{\partial \widehat{u}_t}\Big(\frac{\partial E^{\mu}_{KL}}{\partial \widehat{u}_m}\Big) = \frac{1}{2}\Big(\frac{\partial (F^{\mu}_{Kp})^T}{\partial \widehat{u}_m}\frac{\partial F^{\mu}_{pL}}{\partial \widehat{u}_t} + \frac{\partial (F^{\mu}_{Kp})^T}{\partial \widehat{u}_t}\frac{\partial F^{\mu}_{pL}}{\partial \widehat{u}_m}\Big). \tag{C.8}$$

The material tangent stiffness matrix, C^{μ}_{IJKL}, can be computed from the given microscopic constitutive law. The vectorized forms of Eq. (C.1) is associated with the internal force vector, $\boldsymbol{f}^{\mu}_{\text{int}}(\widehat{\boldsymbol{u}})$. Eqs. (C.2) and (C.3) result in the microscale tangent stiffness matrix and its derivatives.